Effect of Processing Consitions on the Development of Morphology in Clay Nanoparticle Filled Nylon 6 Fibers

Zeynep Ergungor, Miko Cakmak[*]*, Celal Batur*[+]

Polymer Engineering Institute*, Mechanical Engineering Department[+]
University of Akron, Akron, OH, 44325-0301, USA

Summary: The effect of melt temperature on the phase behavior and preferential orientation development in Nylon 6/montmorillonite nanocomposites were investigated at melt spinning temperatures ranging from 230° to 250°C. The fibers were found to exhibit mostly γ crystalline form that is typical of Nylon 6 filled with montmorillonite nanoparticles. At higher take-up speeds α-crystals begin to appear in the crystalline phase. The presence of nanoparticles was found to impart substantial chain orientation levels even at low to moderate take up speeds reaching a plateau at moderate take up speeds. This was attributed to the increased spin line stress in the presence of nanoparticles that increase the overall viscosity due to their large contact areas with the polymer chains. This increased spinline tension was found to cause fiber breakup at moderate speeds. Increasing melt temperature from 230° to 250°C alleviated this problem.

Introduction

Nylon 6 fibers find numerous applications in the industry and their properties have been studied extensively [1,2,3,4,5,6,7]. The fiber structure formation depends primarily on the take-up velocity as well as post spinning process conditions employed. The level of orientation, consequently the birefringence, crystallinity and crystalline perfection increase with take-up velocity and draw down ratio [1,2,4,5,8]. Spinning conditions also affect the crystalline phase nylon 6 filaments assume. Some researchers [4,9] reported that the content of α-phase increases with take-up speed, while the others [5,8,10] argued that the content of γ-phase is higher at higher take-up velocities. The melt extrusion temperature, polymer molecular weight are among the other factors that influence fiber structure formation [2,11,12,13].

It is common practice to embed reinforcing agents (fillers) in a continuous polymeric matrix to improve the performance of polymers. The so-formed macrocomposites improve the thermal and mechanical properties of the original matrix with increasing filler content. However, most of these macro fillers are unsuitable for fiber spinning as they can easily lead to spin line failures due to their size that approach the order of the diameter of the fibers themselves.

Nanocomposites are organic-inorganic hybrids that when broken down to their smallest constituents exhibit very thin and flat particles of nanometer in thickness and much larger

 CCC 1022-1360/00/$ 17.50+.50/0

sizes in the other two dimensions. Because of this substantially reduced thickness and extremely large aspect ratio, the interaction between the filler and polymer is maximized due to the increase in contact area[14]. Consequently the nanofiller concentration could be reduced to 2-5% while providing similar property enhancement as the macrocomposites at substantially high concentrations (e.g. 10-30%)[14]. Because of this, nanofillers add significant value to the final products including weight savings (as compared to macrofillers) and better processability. Clay and layered silicate type nanoparticles are readily found in nature and they have been used and studied extensively. These platelet type particles when homogeneously dispersed in the nylon matrix enhance the Young's modulus and tensile strength, increase the thermal stability, gas barrier properties and offer better flame retardancy relative to pure nylon 6 materials [15,16,17].

Studies on the nylon 6-clay nanocomposite fibers are limited [9,18,19]. Giza et al. [9] compared the fiber structures in pure nylon, and nylon 6-clay hybrids with 2 and 5 wt% clay content. The nanocomposites displayed higher crystallinity in the whole take-up velocity range (1-5 km/min) and higher birefringence (up to 3 km/min) compared to nylon 6 fibers. Orientation induced crystallization started at lower take-up speeds (2 km/min for the nanocomposite versus 4 km/min for nylon 6) and resulted in the direct formation of the crystals of α-form. In a following paper, Giza et al. [18] produced neat nylon 6 and nanocomposite fibers by in-line drawing process where the high-speed melt spinning and drawing processes are combined in one operation. Hybrid fibers displayed higher crystallinity, higher content of α phase as well as higher modulus, although they resulted in lower molecular orientation compared to pure nylon 6 filaments.

In this study, the thermal properties, orientation and structural changes of nylon 6 nanocomposites are investigated as a function of melt temperature. Hot stage WAXS experiments are conducted to elucidate the nature of different melting peaks observed in DSC scans.

Experimental

Materials and Spinning Conditions

Pellets of experimental nylon 6 packaging grade melt compounded nanocomposite (Capron® XA-2744) were kindly provided by Honeywell Corporation. The pellets were dried for 24 hr. in a vacuum oven at 80°C prior to spinning. Melt spinning was carried out using Instron capillary rheometer. Filaments were extruded at 3 different temperatures: 230°, 240° and 250°C at a constant extrusion rate of 0.1''/min ($25.4*10^{-2}$ m/min). Fibers extruded through the

die with a diameter of 0.06273'' ($1.6*10^{-3}$ m) were taken up. However, at each extrusion temperature, breakage of the spinline limited our fiber collection. These critical limits were reached around 40, 120 and 170 m/min for spinning temperatures of 230°, 240° and 250°C respectively. Shimuzu et al. [5] have reported that especially at take-up velocities less than 2,000 m/min, birefringence of the fibers increases substantially within an hour after spinning due to the crystallization induced by moisture in the air. The fibers were then conditioned for at least 1 week prior to any testing.

Differential Scanning Calorimetry

The differential scanning calorimetry (DSC) measurements were carried out using a Dupont TA 2920. The samples weighing in the range of 5±0.4 mg were cut into small pieces, crimped in aluminum sample holders, heated from 40°C to 300°C at a heating rate of 10°C/min under a nitrogen blanket.

Birefringence

The retardation of as-spun fibers was determined using a leitz Laborlux 12 Pol S optical microscope, equipped with a 20X analyzer eyepiece and a Berec compensator. The birefringence was calculated by dividing the retardation of the fibers by their diameter. The average of the measurements for six individual fibers is reported.

Wide Angle X-Ray Experiments

Wide angle X-ray scattering diffractometer scanning ($\theta/2\theta$ in reflection mode) was performed using 15 kW Rigaku RU-200B operated at 50kV and 150 mA. The hot stage was programmed to heat from 45° to 190°C at 30°C/min and from 190° to 250°C at 10°C/min. The WAXS profiles were obtained at 190°, 212°, 232°, 242° and 250°C. Each scan was recorded in the $2\theta = 2.5^0$-28^0 range, at a scanning rate of 2^0/min and 0.05^0 sampling interval.

We obtained the WAXS flat film patterns using a General Electric generator equipped with a pinhole type (transmission) camera. The incident X-ray beams were monochromatized with nickel foil filter to obtain CuK_α radiation with single wavelength of 1.54178 Å. The sample-to-film distance was 3.26 cm.

Orientation Measurements

Crystalline orientations of the monoclinic γ phase were calculated from the equation of Wilchinsky [20] using the crystallographic data of Arimoto et al. [21]. We obtained:

$$\langle \cos^2 \phi_{c,z} \rangle = 1.36 \langle \cos^2 \phi_{001,z} \rangle$$

where the integrated peak intensity for the (001) reflection of the γ form was calculated as a function of azimuthal angle in the 0^0-360^0 range from radial densitometer scans on the WAXS

films, performed every 1^0. Then the Hermans-Stein orientation functions were calculated from the equatorial reflection [22,23]:

$$f_c = \frac{3}{2}\langle \cos^2\phi_{c,z}\rangle - \frac{1}{2} = 2.04\langle \cos^2\phi_{001,z}\rangle - \frac{1}{2} \quad (1)$$

and assuming fiber symmetry by:

$$f_b = -2f_c = -2f_a \quad (2)$$

Results and Discussion

Rheological Properties

The shear viscosity measurements were performed using Instron capillary rheometer at 230°, 240° and 250°C. The viscosity of the melt-compounded nanocomposite at these three temperatures is plotted as a function of shear rate in Figure 1. The melt compounded nylon 6 nanocomposite material displays shear thinning behavior as reported previously [24]. At a given shear rate the shear viscosity is higher at the lower temperature as expected.

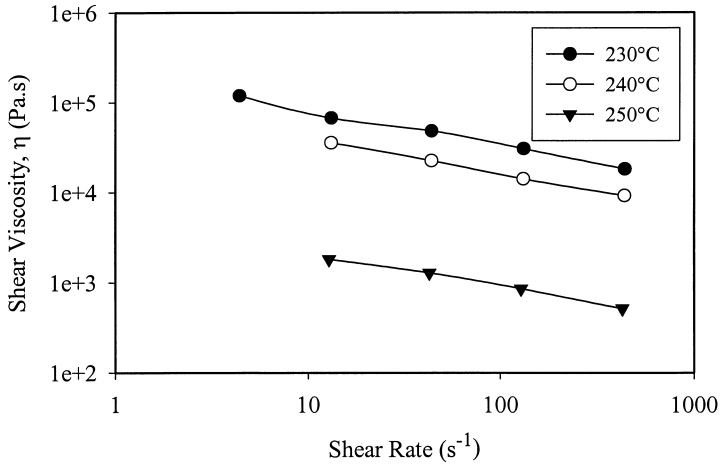

Figure 1. Shear Viscosity of Melt Compounded Nanocomposite Materials at Different Melt Temperatures. The labeling indicates the melt temperature for the nanocomposite pellets.

Differential Scanning Calorimetry (DSC) Studies

The DSC scan of the as received pellet is given in Figure 2. The exothermic and endothermic transitions of the nanocomposites display some interesting features. Following the broad dehydration peak in the 75°-180°C region, an exothermic peak is observed just below the melting region (195°C). As explained by Khanna[25], low crystallinity nylon 6 may exhibit a sub-T_m exothermic transition of varying breadth and intensity depending on the processing conditions during production. These operations require fast cooling processes inducing high stresses. This sub-T_m peak could then characterize such a transition where processing-induced stresses are relaxed. Reorganization of unstable crystals into a more stable form could also result in such a transition [7,26,27]. At higher temperatures, three endothermic peaks are observed at 211°, 221° and 238°C. Usually the melting temperature of nylon 6 is noted as 215-222°C [3]. We will first discuss the origin of the two lower temperature endothermic peaks. Double melting peaks similar to peak 1 and peak 2 in Figure 2 have been observed for some nylon 6 [28,29] and some nylon 6 nanocomposites [30,31]. However, there are contradictory explanations on the nature of such melting peaks. First, some researchers suggest that these peaks correspond to the α and γ phases of nylon 6, with the lower temperature peak representing the melting temperature of the γ phase [30,31]. Second, some studies show that

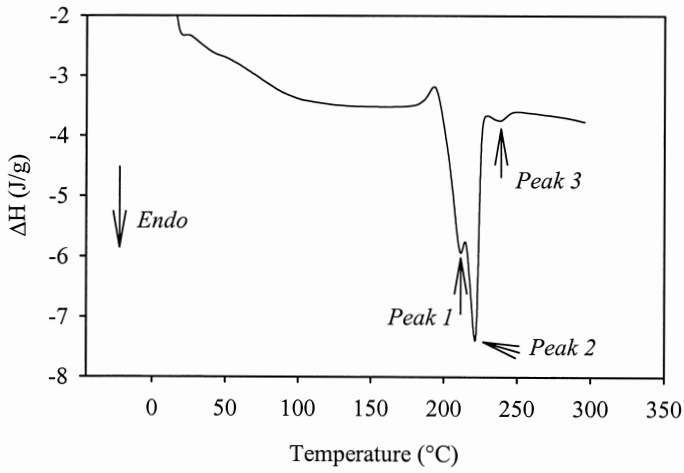

Figure 2. Thermal Properties of the As-received Nylon 6 Nanocomposite Pellets. Peak 1, peak 2 and peak 3 refer to the three endothermic transitions mentioned in the text.

these double melting peaks correspond to the superposition of different processes that occur during DSC heating [28,29]. Todoki et al. [28] claim that the original polymer crystals perfect and melt at a lower temperature, then recrystallization occurs and recrystallized crystals melt at a higher temperature. Itoh et al. [29] consider an intermediate phase with intermediate thermal properties and structure between the crystalline and liquid amorphous phases. According to them, the crystalline phase melts at the lower temperature. The recrystallization and melting of the intermediate phase contribute to the peak at the higher temperature. Third, it is also known that population of distinct sized and/or shaped crystals causes different melting peaks with smaller (and possibly more internal disorder) crystals melting at a lower temperature.

The presence of a third melting peak, at even a higher temperature than those mentioned above, is not common. However, Koshitsugu et al. [32] observed a characteristic peak at 240°C in the nylon 6-clay hybrids annealed under elevated pressure (0.15-0.3 GPa, at 260°C and 1 hr) in addition to two endothermic peaks at 208°C and 223°C. They categorize the nylon 6 in the hybrid as bonding (nylon ionically bound to the clay) and nonbonding nylon. They explain that the bonding nylon, which has a lower molecular weight, rearranges into larger crystallites and melts at a higher temperature. We observe this third peak for the as received pellets which are not subjected to any treatment by us, then we can conclude that this peak emerged as a result of some treatment at or after the production, but before we received it.

In order to elucidate the mechanisms responsible for these peaks, hot stage-WAXS experiments are performed. For this series of experiments, nylon 6 nanocomposite pellets were compression molded at 240°C. The WAXS profiles of these samples were recorded at regular temperature intervals from room temperature up to 250°C (Figure 3) as explained in the experimental section.

According to the scan at 30 °C, the nylon 6 nanocomposite under investigation is γ-phase dominant. The peak of the 001 plane of the γ-phase appears at 21.65^0. The shoulder observed around 2θ of 19^0 might be the result of the broad peak of the amorphous phase around $2\theta = 20^0$. The small peak at $2\theta = 24.5^0$ represents the (002)/(202) peak of the α-phase. Therefore at the beginning the structure is mainly in γ-phase but some α-form is also present. The absence of a diffraction peak representing clay at small diffraction angles (below $2\theta = 5^0$) indicates that the nanocomposite is exfoliated or has a very disordered structure.

As the temperature is increased to 190°C, the (001) γ-peak shifts to 20.9^0 and a shoulder appears at 20.65^0. At 212°C, the shoulder at 20.65^0 becomes more prominent around 20.55^0.

This peak corresponds to the (200) peak of the α-form crystals, which becomes significant at

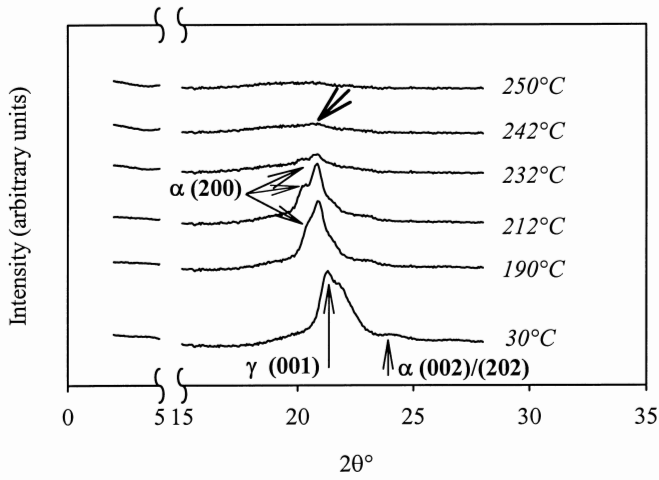

Figure 3. Hot Stage WAXS of Compression Molded Samples.
Scans were performed at each temperature indicated.
The characterization of each intensity peak is indicated as well.

such high temperatures by recrystallization. The small peak representing the (002)/(202) peak of the α-phase shifts to $2\theta = 23.1^0$. At this point we want to emphasize that the sample for this series of experiments is exposed to high temperatures for longer times (each scan lasts approximately 13 minutes) as compared to the DSC samples (see the experimental conditions). For this reason, the emergence of the α-phase in the hot stage experiments does not require the formation (and) at the same amount of α crystals in the DSC experiments.

At 232°C, the (200) peak for the α and the (001) peak for the γ phase are still discernible although their intensities are substantially diminished. All the peaks relating to the α-phase disappear at 242°C, while the (001) peak of the γ-structure is still discernible (as indicated by the bold arrow). The (001) γ-peak ultimately disappears at 250°C. We can then conclude that the nylon nanocomposite preserves the dominant γ-phase structure from room temperature up to 250°C. In addition to a small amount of α- crystals that are present at the beginning of the scan, additional crystallization in α-form occurs near 190°C. These crystals eventually melt around 240°C. At 250°C, the amorphous molten polymer dominates the WAXS intensity profile.

The next question then is: why don't all the crystals melt in the 190°-230°C temperature range but a third melting peak emerges above these main double melting peaks? Based on the DSC

scan in Figure 2, the area under the main melting endotherms (under peaks 1 and 2) is nearly 10 times the area under the third melting peak at 240°C. Then the material melting at very high temperatures constitute a very small portion of the polymer. Although WAXS experiments indicate the presence of exfoliated nanocomposite morphology, silicate layer distribution may still not be uniform. A small fraction of aggregates containing more than one layer can be present. The presence of silicate aggregates obviously further stabilizes a γ-crystal structure, which persists until very high temperatures (the (001) peak of the γ-structure is still discernible at 242°C, Figure 3). At temperatures beyond the usual melting temperature, the high melting nylon 6 γ- crystals, originally protected by and trapped between the small fraction of aggregates are released and finally melt (it is probable that at this high temperature the clay platelets don't present ordering characteristic of layer correlation anymore). Additionally, it is stated that in melt compounded nanocomposites, polymer chains interact weakly with the silicate layer and indicate the formation of more defect-ridden crystallites [33,34]. The most perfect crystallites situated in between the silicate aggregates could then be melting beyond the melting temperature of the bulk polymer. The illustration of this theory is given in Figure 4.

The DSC scans of the nylon 6 nanocomposite fibers spun at 240°C and at different take-up speeds are given in Figure 5. The behavior of the fibers spun at 230°C and 250°C follow the trends we will discuss on Figure 5. At the lowest take-up speed (2.6 m/min), three melting peaks are observed at 210°, 221° and 250°C. As the take-up speed increases the temperature of the first peak shifts to higher temperature and its area decreases. While its position is fixed, the area of the second melting peak increases at higher take-up speeds. The increase in take-up speed, thus improved chain orientation promotes recrystallization and perfection of the crystals. Consequently, there are more and more perfect crystals, which melt at higher temperatures at increased take-up speeds (see the discussion in the Wide Angle X-ray Diffraction section for the perfection of crystals). On the other hand, the area and peak position of the third melting peak are constant, most likely because the amount of nylon 6 constrained between montmorillonite aggregates does not vary depending on the processing conditions. Moreover, we depict a fourth peak around 235.4°C (peak numbered 4). One possible explanation for the appearance of this peak is recrystallization and melting of even a more distinct population of crystals beyond the main melting peaks. Another explanation is the melting of, at this point unconstrained nylon 6 in two steps, at 235.4° and finally at 250°C.

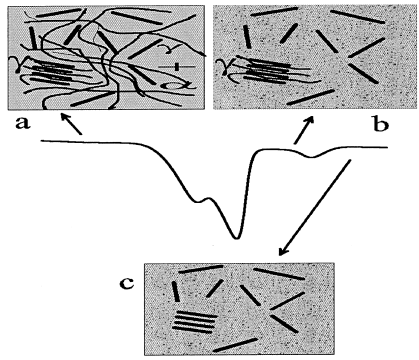

Figure 4. The Thermal Behavior of Nylon 6 Nanocomposites. a) Below the main melting peaks, a very small portion of the polymer (γ-phase) is trapped in silicate layer aggregates. b) Just above the main melting endotherms, the bulk polymer is molten but some γ-phase polymer is still inside the aggregates. c) Beyond the third melting peak, the entire polymer is finally molten.

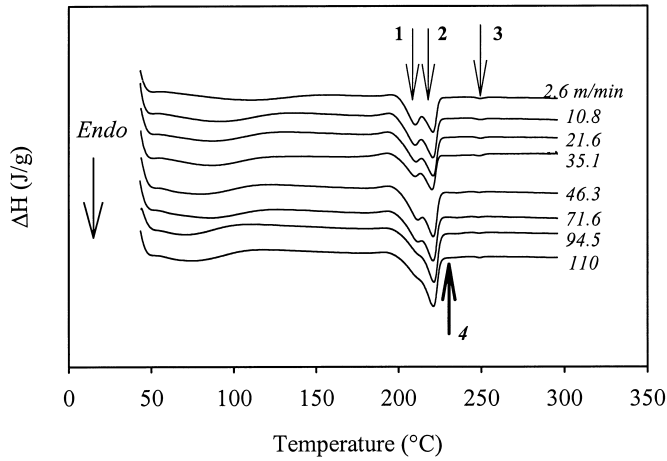

Figure 5. Thermal Behavior of Fibers Spun at 240°C.
The take-up speeds are indicated next to each figure.
The peak numbers as referred in the text are indicated.

Crystallinity from DCS Measurements

Figure 6 summarizes the crystallinity of nylon 6 nanocomposite fibers. Crystallinity is usually calculated from the heat of fusion recorded by DSC scans according to:

$$\%Crystallinity = \frac{\Delta H_{melt} - \Delta H_{crys}}{\Delta H_{\infty}} \qquad (3)$$

where ΔH_{melt} is the endothermic heat flow due to melting, ΔH_{crys} is the exothermic heat flow due to crystallinity and ΔH is the heat of fusion of the 100% crystalline material. The broad dehydration peak prevents us from detecting any possible cold crystallization peaks. However the crystallinity is calculated correctly by subtracting the area of the sub-T_m peak from the melting region area as discussed by Khanna et al. [25] Although some α-phase is present at the highest take-up speeds (see the Wide Angle X-ray Diffraction section), for calculation purposes we consider only the heat of fusion of the 100% γ- phase (ΔH = 213 J/g [35]).

High take-up velocities lead to increased molecular orientation in the fiber prior to solidification, which in turn causes increased crystallization rates and increased crystallinity development during the spinning process. Consequently, as the take-up velocity increases crystallinity of the fibers increases as shown in Figure 6. Similarly, spinline stress directly affects the orientation levels[1]. Spinning stress, which is the ratio of the take-up force to the fiber cross section, decreases as the spinning temperature increases. Then, at a given take-up speed, crystallinity is lower for the fibers spun at a higher temperature.

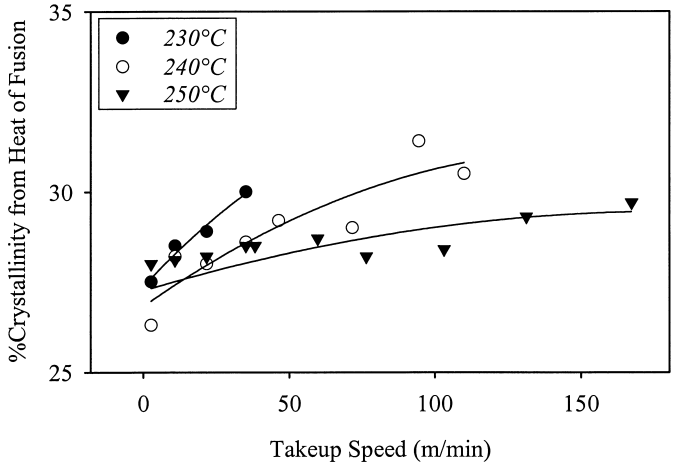

Figure 6. Percent Crystallinity of Fibers as a Function of Take-up Speed. The labeling indicates different spinning temperatures.

Birefringence Measurements

The birefringence of the fibers spun at 230°, 240° and 250°C is plotted as a function of take-up speed and draw down ratio in Figure 7 a-b.

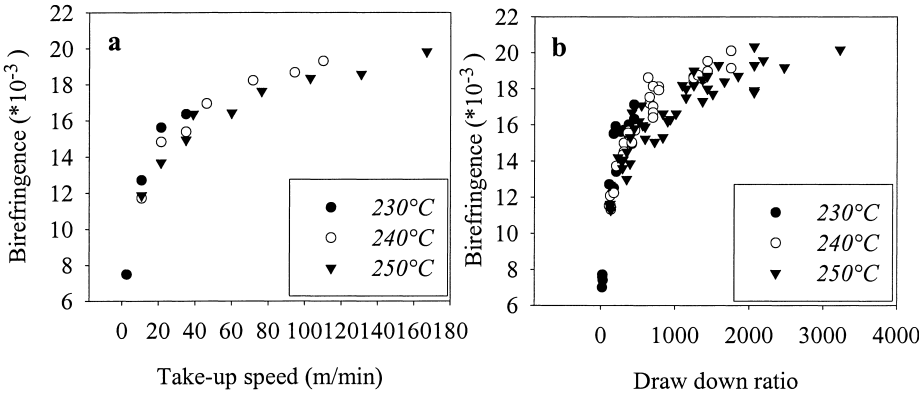

Figure 7. Birefringence of the Fibers Spun at Different Temperatures as a Function of a) Take-up Speed and b) Draw Down Ratio

The draw down ratio (DDR) is defined as $DDR = A_{die} / A_{fiber}$ where A_{die} is the constant cross-sectional area of the die at the exit, A_{fiber} is the cross sectional area of the fiber after conditioning. Increase in draw down ratio is a direct consequence of the decrease in A_{fiber} caused by increased spinline stress when the take-up velocity increases. Increasing the take-up velocity at constant extrusion rate and die dimensions causes an increase in melt draw down and cooling rate of the filament and consequently greater molecular orientation. Consequently, as the take-up speed increases, the birefringence, which is a classical measure of orientation, increases roughly by 50-75%. The same phenomenon is observed for increasing draw down ratios.

The birefringence, although slightly, increases with the decrease in spinning temperature as well, due more readily cooled down filaments and increased spinline stress. For all the fibers spun at different temperatures, the birefringence increases continuously and rapidly at low take-up speeds. Beyond the take-up speed of 40-50 m/min, the birefringence begins to level off. So the fibers reach a practically limiting orientation at take-up velocities as low as 50 m/min where they also reach their maximum strength levels. Beyond this point, the stress on the spinline exceeds this limiting strength levels and spinline breakage occurs.

Wide Angle X-Ray Diffraction Studies

In Figure 8, selected X-ray patterns of the fibers spun at 240°C are given as an example to illustrate the changes that take place in the crystalline phase and orientation with deformation. The crystalline reflections in the WAXS patterns belong to the dominant γ-phase. A mild orientation is observed at low take-up speed and this naturally increases. Only at the highest

take-up speeds attainable without filament rupture, some oriented α-phase becomes discernible. The proportions of areas of the peak 1 and peak 2 obtained from the DSC scans don't correspond to the appearance of phases in X-ray patterns. This is another experimental evidence that the double melting peaks observed in DSC scans don't represent directly the γ and α forms of nylon 6. Giza E. et al. [9] documented that for the pure nylon 6 and nylon 6 nanocomposites α-form crystals are enhanced at sufficiently high take-up velocities. In our case the take-up speeds at which the α-phase is discernible are much lower than the ones recorded in their work for nylon 6 (5 km/min) and nylon 6 nanocomposites (2 km/min). The α-phase appears at lower take-up speeds for lower spinning temperatures where orientation is promoted. For the calculation of crystalline orientation function, only orientation in the γ phase will be taken into account.

In Figure 9, the WAXS 2θ scans of the fibers spun at 240°C with corresponding minimum, intermediate and highest take-up speeds are presented. These results also confirm that at low take-up speeds, the fibers assume γ phase and some α phase is generated at high take-up velocities. At comparable take-up velocities, the amount of α structure formed diminishes as the spinning temperature increases from 230° to 250°C. In summary, especially for the fibers spun at high temperatures only a minor amount of α phase is present (much smaller than necessary to report for the relative ratio of the area of the two endotherms -peak 1 and peak 2- in DSC). Figure 9 also indicates that for the fibers spun at specific temperature, diffraction peaks become broader as the take-up speed increases. This broadness accounts for smaller crystallite size according to the Scherrer equation[36] where the crystallite size is inversely proportional to the breadth at half-maximum intensity of the X-ray reflection profile. The crystallite sizes were calculated from the FWHM (full width-half maximum) of the (001) γ peak determined with the Microcal Origin® program, following peak separation (Table 1).

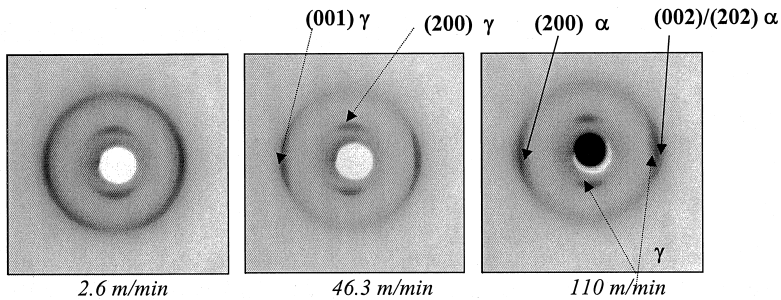

Figure 8. WAXS for Selected Fibers Spun at 240°C.

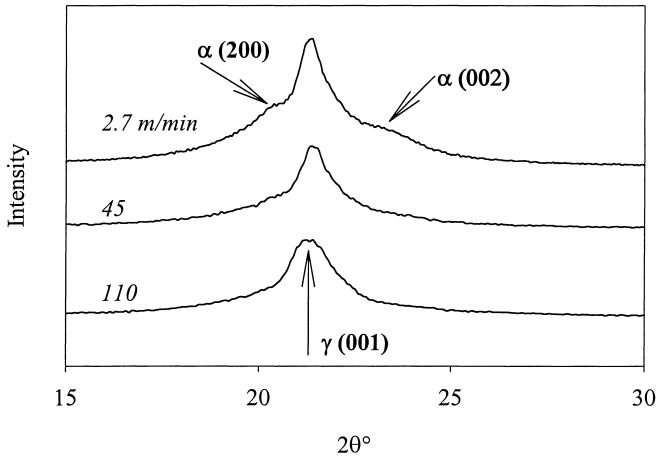

Figure 9. WAXD 2θ Scans of Fibers Spun at 240°C
at Selected Take-up Speeds.

Table 1. Crystallite Sizes of the Fibers Spun at Different Spinning Temperatures (T_s)

Take-up speed (m/min)	Crystallite size (Å) (T_s = 230°C)	Take-up speed (m/min)	Crystallite size (Å) (T_s = 240°C)	Take-up speed (m/min)	Crystallite size (Å) (T_s = 250°C)
2.7	70.43	2.7	77.15	2.6	73.85
10.8	67.05	46.3	73.72	39.1	66.24
35	62.34	110	62.04	167	59.15

Orientation Measurements

The Hermans orientation factors along the a, b, c crystallographic axes are given as a function of take-up speed at the three spinning temperatures in Figure 10. As the take-up speed increases, while the crystalline orientation factor along the chain axis, f_b increases, f_a and f_c decrease. This is a direct consequence of the polymer chain direction becoming more aligned with the fiber axis while the other two directions aligning mostly perpendicular to the fiber axis. Although the differences are not substantial, f_b decreases as the spinning temperature increases, due to decreased take-up stress. Correspondingly, f_a and f_c increase very slightly as the spinning temperature increases. The orientation interpreted from Hermans orientation function also begins to level off around the same take-up speed as detected from birefringence calculations (40-50 m/min).

The total birefringence represents the sum of crystalline and amorphous contributions. From our birefringence and crystalline orientation functions we were able to calculate the amorphous orientation function f_{am} by[37]:

$$\Delta n = X f_c \Delta_c^0 + (1 - X) f_{am} \Delta_{am}^0 + \Delta n_{form} \quad (4)$$

where Δn is the in-plane birefringence, X is the crystalline fraction, f_c and f_{am} are the Hermans orientation factors for the crystalline and amorphous phases respectively; Δ_c^0 and Δ_{am}^0 are the intrinsic birefringences of crystalline and amorphous phases; and Δn_{form} is form birefringence. In nylon 6, the chains are aligned along the crystallographic b axis, so for our materials f_c will be represented by f_b calculated previously. The contribution of the α-form crystals to the total birefringence, if any, will be neglected. The form birefringence Δn_{form} that could be arising due to optical contrast between the polymer and filler is neglected. The crystalline and amorphous intrinsic birefringences are estimated to be $\Delta_c^0 = 0.078$[38] and $\Delta_{am}^0 = 0.064$[39] respectively.

In Figure 11, the amorphous orientation function f_{am} is plotted as a function of take-up velocity at three spinning temperatures. We can see that f_{am} increases as the take-up speed increases and as the spinning temperature decreases. Thus, as the take-up velocity increases, the orientation improves in both crystalline and amorphous regions.

Structural Interpretation

The presence of nanoparticles plays a number of significant roles in the evolution of structure in the nylon 6 fibers. It is clear from the as received materials that the clay nanoparticles promote the formation of γ crystal form upon crystallization from the melt. We also observed that some of the nylon 6 chains, presumably trapped in between the solid walls of the nanoparticles that are in close proximity with one another, survive to higher temperatures as evidenced in the DSC curves as a distinct melting peak. The hot stage WAXS studies confirmed that these chains are in γ crystalline form that is known to be promoted by the clay nanoparticle. Fiber spinning was found to quickly orient the polymer chains in the crystalline and amorphous regions. A significant portion of this orientation is as a result of the presence of nanoparticles that locally increase the stresses that in turn help develop the orientation quickly. The evidence on this local effect is reflected in the published rheological properties of such systems [14,40] that indicate significant increases in the viscosity in the presence of

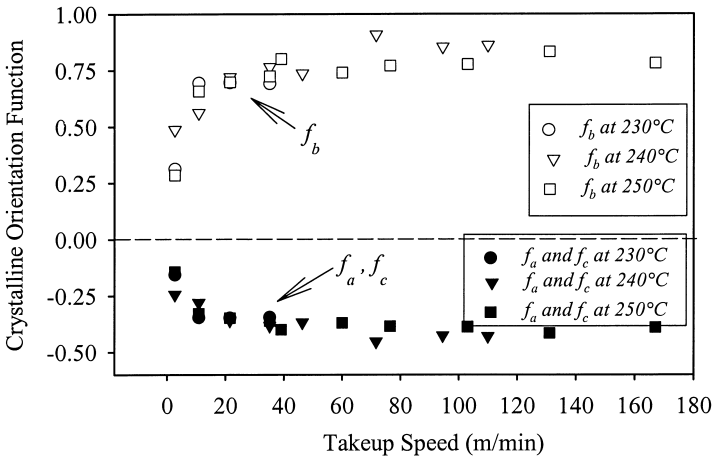

Figure 10. Hermans Orientation Functions Along the Three Crystallographic Axes. b is the chain axis. The spinning temperatures are indicated in label.

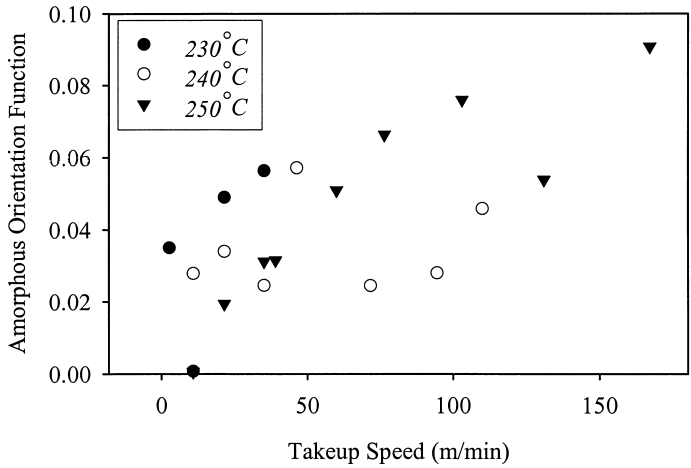

Figure 11. Amorphous Orientation Function of the Fibers as a Function of Take-up Speed. The spinning temperatures are indicated in the label.

nanoparticles at very low (3-5 %) concentrations. The type of flow also plays an important role on the orientation of the fiber along the spinline. The fiber at the exit of the die is still under the influence of shear flow in the capillary. Down the spinline, the elongational flow takes over the shear flow for the bulk polymer. The polymer chains situated in between the clay platelets on the other hand are oriented when subjected to two types of flow: First, elongational flow is significant due to take-up. In addition, small relative motion of adjacent nanoparticles result in significant shearing in the chains situated in the space between them leading to amplification of the shearing in such small spaces. Additionally, the silicate layers also become aligned and oriented with the flow along the fiber axis even at the lowest take-up speed as indicated by the Small Angle X-Ray Scattering in Figure 12a. This orientation is clearly observed at the high take-up speeds as well (Figure 12b).

It is important to note that the orientation of the crystalline regions correlate well with the total deformation as represented by draw down ratio and it is not sensitive to the melt temperature while the orientation of the amorphous regions are sensitive to the melt temperature utilized-being higher at lower melt temperatures as expected. These mechanisms are graphically depicted in Figure 13.

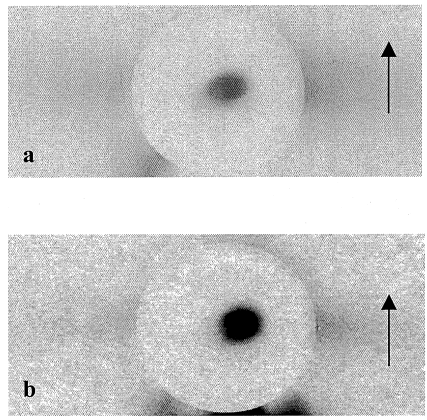

Figure 12. SAXS of the fibers spun at 240°C at the
a) lowest (2.6 m/min) and b) highest take-up speeds
(110 m/min). The arrow indicates the fiber axis.

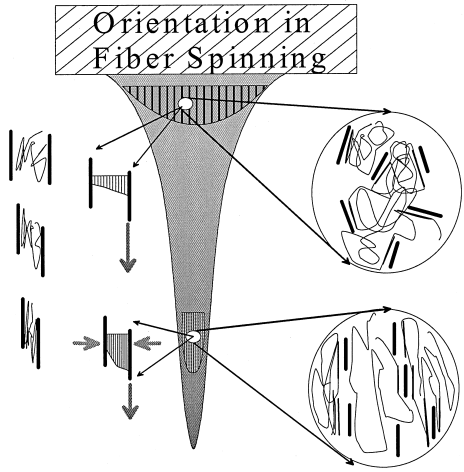

Figure 13. Effect of Nanoparticles and Type of Flow on Orientation Development During Fiber Spinning of Nanocomposite Materials.

Conclusions

We have shown that the presence of small amount of nanoparticles significantly enhances the orientation levels in the spun fibers at small to moderate take up speeds. Since the clay particles promote high orientation levels, they reach their plateau strength levels at moderate deformation levels. This is very similar behavior to what was observed in the spinning of thermotropic liquid crystalline polymers that are well known to exhibit high orientation levels and exhibit very long orientation relaxation times. The presence of such chemically "unconnected" nanoparticles play a similar role of suppressing the orientation relaxation while promoting the orientation by the "shear amplification" mechanism that occurs in the small spaces between the adjacent clay particles where small relative motion of the particles greatly amplifies the shearing effects. The crystalline orientation is primarily controlled by the total deformation of the fiber with little or no sensitivity to the melt temperature. The amorphous chain orientation, on the other hand, exhibited expected melt temperature dependency – being higher at lower melt temperatures.

Acknowledgements

We would like to thank University of Akron Research Office for providing support for Z. Ergungor.

[1] A. Ziabicki, K. Kedzierska, *J. Appl. Polym. Sci.* **1962**, *6*, 111.
[2] T. Ishibashi, K. Aoki and T. Ishii, *J. Appl. Polym. Sci.* **1970**, *14*, 1597.
[3] M.I. Kohan, Ed. "*Nylon Plastics*", Wiley-Interscience, New York 1973.
[4] V. G. Bankar, J.E. Spruiell, J.L. White, *J. Appl. Polym. Sci.* **1977**, *21*, 2341.
[5] J. Shimizu, N. Okui, T. Kikutani, A. Ono, A. Takaku, *Sen'i Gakkaishi* **1981**, *37*, 37.
[6] J. L. White, M. Cakmak, *Adv. Polym. Tech.* **1986**, *6*, 295.
[7] M. Jaffe, J.D. Menczel, W.E. Bessey in: "*Thermal Characterization of Polymeric Materials*", Vol. 2, E. A. Turi, Ed., Academic Press, CA 1997.
[8] R. F. Stepaniak, A. Garton, D.J. Carlsson, D.M. Wiles, *J. Appl. Polym. Sci.* **1979**, *23*, 1747.
[9] E. Giza, H. Ito, T. Kikutani, N. Okui, *J. Macromol. Sci. Phys.* Part B, **2000**, *39*, 545.
[10] J. Gianchandi, J.E. Spruiell, E.S. Clark, *J. Appl. Polym. Sci.* **1982**, *27*, 3527.
[11] S. Kaufman, *Chem. Vlakna* **1971**, *21*, 202.
[12] J.H. Baheda, J.E. Spruiell, *J. Appl. Polym.Sci.*, **1990**, *39*, 447.
[13] K. Koyama, J. Suryadevara, J.E. Spuriell, *J. Appl. Polym. Sci.*, **1986**, *31*, 2203.
[14] M. Alexandre, P. Dubois, *Mat. Sci. Eng.* **2000**, *28*, 1.
[15] A. Usuki, A. Koiwai, Y. Kojima, M. Kawasumi, A. Okada, T. Kurauchi, O. Kamigaito, *J. Appl. Polym. Sci.* **1995**, *55*, 119.
[16] L.A. Goettler, D.W. Recktenwald, "*Nylon nanocomposites: Performance attributes and Potential Applications*". Addit. '98, Int. Conf. Exhib., 7th, 1998.
[17] J.W. Gilman, A. Morgan, E. Giannelis, M. Wuthenow, E. Manias, Flame Retardancy, 10th Annual BCC Conference Proceedings, Stamford, CT, 1-11 1999.
[18] E. Giza, H. Ito, T. Kikutani, N. Okui, *J. Polym. Eng.* **2000**, *20*, 403.
[19] N. Ogata, S. Kawakage, T. Ogawa, T. Yanagawa, T. Ogihara, *Sen'i Gakkaishi*, **1996**, *52*, 457.
[20] Z.W. Wilchinsky, *J. Appl. Phys.*, **1959**, *30*, 792.
[21] H. Arimoto, M. Ishibashi, M. Hirai, Y. Chitani, *J. Polym. Sci.*, Part A **1965**, *3*, 317.
[22] P.H. Hermans, P. Platzek, *Kolloid Z.* **1939**, *88*, 68.
[23] R. S. Stein, *J. Polym. Sci.* **1958**, *31*, 327.
[24] J.W. Chao, D.R. Paul, *Polymer* **2001**, *42*, 1083.
[25] Y.P. Khanna, W.P. Kuhn, *J. Polym. Sci.*, Part B **1997**, *35*, 2219.
[26] N. Hiramatsu, S. Hirakawa, *Polym. J.* **1982**, *14*, 165.
[27] M. Kyotani, *J. Macromol. Sci. Phys.* **1975**, *B11*, 509.
[28] M. Todoki, T. Kawaguchi, *J. Polym. Sci., Polym. Phys.* **1977**, *15*, 1067.
[29] T. Itoh, H. Miyaji, K. Asai, *Jap. J. of Appl. Phys.* **1975**, *14*, 206.
[30] L. Liu, X. Zhu, Z. Qi, *Gaofenzi Xuebao*, **1999**, *3*, 274.
[31] T. Wu, C. Liao, *Macrom. Chem. Phys.* **2000**, *201*, 2820.
[32] Y. Kojima, T. Matsuoka, H. Takahashi, T. Kurauchi, *J. Appl. Polym. Sci.* **1994**, *51*, 683.
[33] D.M. Lincoln, R.A. Vaia, Z.-G. Wang, B.S. Hsiao, *Polymer* **2001**, *42*, 1621.
[34] D.M. Lincoln, R.A. Vaia, Z.-G. Wang, B.S. Hsiao, R. Krishnamoorti, *Polymer* **2001**, *42*, 9975.
[35] Y. Kojima, A. Usuki, M. Kawasumi, A. Okada, T. Kurauchi, O. Kamigaito, K. Kaji, *J. Polym. Sci., Part B* **1994**, *32*, 625.
[36] L.E. Alexander, "*X-Ray Diffraction Methods in Polymer Science*", Wiley-Interscience, New York 1969.
[37] M. Born, E. Wolf, "*Principle of Optics*", Pergamon, Oxford 1970.
[38] F. Nagatoshi, T. Arakawa, *Polym. J.* **1970**, *1*, 685.
[39] E. Balcerzyk, W. Kozlowski, E. Wesolowska, W. W. Lewaszkie, *J. Appl. Polym. Sci.* **1981**, *26*, 2573.
[40] E.P. Giannelis, R. Khrishnamoorti, E. Manias, *Adv. Polym. Sci.* **1999**, *138*, 107.